EDGE ARTICLE
Tomoki Nishimura *et al.*
Self-assembled block copolymer domains as
macromolecular ion transport systems in biological
membranes

15 YEARS ANNIVERSARY

Check for updates

Self-assembled block copolymer domains as macromolecular ion transport systems in biological membranes

Shunji Kosaka,[a] Jokichi Fukushima,[a] Nanami Takeuchi, [b] Noriko Miyamoto,[c] Liliana de Campo,[d] Ryuji Kawano [b] and Tomoki Nishimura [*a]

Synthetic ion channels represent an emerging class of therapeutics. However, most synthetic ion channels are derived from small molecules, whose rapid clearance from the body limits their therapeutic potential. Here, we report macromolecular ion transport systems based on amphiphilic polyether block copolymers. The block copolymers self-assemble into vesicles that are spontaneously incorporated into biological membranes to form polymer-rich domains. The hydrophobic core of the domains, which features ether–oxygen atoms and the presence of water molecules, is analogous to the permeation pathways of natural ion channels such as KcsA. In addition, the inherent thermoresponsive properties of these polymer domains enable on/off switching of ion transport in response to temperature variations, allowing for controlled modulation of cation permeability. Thus, these domains act as macromolecular ion transport systems to disrupt ion homeostasis and trigger apoptosis in cancer cells. The systemic administration of the vesicles in tumor-bearing mice resulted in an accumulation at the tumor sites, inhibiting tumor growth. This work establishes thermoresponsive polyether block copolymers as a versatile and biologically active platform for macromolecular ion transport systems.

Introduction

Natural ion channels play a central role in maintaining cellular homeostasis by regulating ion gradients across biological membranes.[1] Inspired by these functions, synthetic ion channels have been developed as mimetic systems of natural ion channels.[2–8] Synthetic channels with features such as superior ion selectivity,[9–11] high transport efficiency,[12,13] control through external stimuli,[14–22] and multistate conductance[23] have been achieved. These synthetic ion channels can be introduced into cancer cells to disrupt ion homeostasis and induce apoptosis, and thus represent a novel approach to cancer treatment.[24–31]

Despite these achievements, most synthetic ion channels developed to date are based on small molecules and are rapidly excreted by the kidneys when administered systemically.[32–34] This significantly reduces their overall bioavailability and limits their therapeutic efficacy. In contrast, polymer-based systems offer a promising solution: their nanoscale assemblies not only

aDepartment of Chemistry and Materials Science, Shinshu University, 3-15-1, Tokida, Ueda, Nagano 386-8567, Japan. E-mail: nishimura_tomoki@shinshu-u.ac.jp

bDepartment of Biotechnology and Life Science, Tokyo University of Agriculture and Technology, Tokyo 185-8588, Japan

cDepartment of Applied Chemistry, Faculty of Engineering, Aichi Institute of Technology, 1247, Yachigusa, Yakusa-cho, Toyota, Aichi, 470-0392, Japan

dAustralian Centre for Neutron Scattering, Australian Nuclear Science and Technology Organisation (ANSTO), New Illawarra Road, Lucas Heights, NSW 2234, Australia

accumulate at tumor sites *via* the enhanced permeability and retention (EPR) effect but also avoid rapid renal clearance, thereby improving systemic retention and therapeutic potential.[35–40] Nevertheless, maintaining both efficient ion transport and functional integration into biological membranes remains a major challenge. In particular, the ability of polymeric systems to stably incorporate into lipid membranes while preserving ion transport functionality is critical for therapeutic success.

To address this, one strategy to enhance the functionality of biological membranes involves the incorporation of synthetic block copolymers, leading to the formation of polymer/phospholipid hybrid vesicles. Within these hybrid systems, block copolymers can organize into distinct membrane domains, such as laterally phase-separated patches, disk-like inclusions, or raft-like structures.[41–47] The formation and morphology of these domains are governed by several physicochemical factors, including the hydrophobic mismatch between polymer and lipid components, differences in membrane thickness, polymer–lipid miscibility, and the resulting line tension at domain boundaries.[48] Such mesoscale organization is known to modulate membrane curvature, fluidity, and permeability, and has been exploited in previous studies to control molecular transport and membrane-associated functions.

Here, we present a strategy to achieve ion transport through self-assembled polymer domains embedded within biological

membranes. Specifically, we employ amphiphilic block copolymers composed of triethylene-glycol-functionalized poly(glutamate) and poly(propylene oxide) (poly(EG$_3$Glu)-b-PPO), which self-assemble into vesicles and are spontaneously incorporated into lipid and cellular membranes. These domains recapitulate key features of natural ion channels such as KcsA (Fig. 1a)[49–52] by providing ether-rich hydrophobic cores with confined water molecules, enabling cation transport without defined pores (Fig. 1b). Furthermore, the thermoresponsive nature of PPO allows temperature-dependent modulation of ion transport.[53–55] Through this design, we demonstrate that these block copolymer domains function as macromolecular ion transport systems, disrupting ion homeostasis and inducing apoptosis in cancer cells. Systemic administration in tumor-bearing mice results in selective accumulation at tumor sites and significant tumor growth inhibition. While a previous study reported enhanced ion permeability in polymer–lipid hybrid vesicles attributed to size mismatch,[56] the underlying mechanism was not structurally elucidated. In contrast, our work provides direct evidence that self-assembled polymer-rich domains embedded within biological membranes can facilitate ion transport by mimicking the hydration features of natural channels. This represents a distinct and structurally supported design strategy for polymer-mediated ion transport in membranes. Our findings broaden the scope of synthetic ion transport systems and establish a generalizable design principle for engineering polymer-based ion transport platforms across diverse membrane systems.

Results and discussion

Design and synthesis of the amphiphilic block copolymers

To enhance compatibility with lipid bilayers, we designed relatively low-molecular-weight block copolymers. This is because excessive hydrophobic mismatch and significant differences in bilayer thickness can hinder domain formation.[48] Among the hydrophobic blocks, the poly(propylene oxide) (PPO) was selected due to its solubility parameter ($\delta = 16.3$ MPa$^{1/2}$) being similar to that of the hydrophobic core of phospholipid bilayers ($\delta = 17.4$–19.0 MPa$^{1/2}$), which promotes better miscibility. These factors are considered critical for effective domain formation and membrane incorporation in hybrid vesicles.

In addition to membrane miscibility, the chemical structure of a block copolymer can affect both its cation permeability and its ability to incorporate into biological membranes. Thus, we designed and synthesized three amphiphilic block copolymers with various hydrophobic segments, i.e., PPO, poly(butylene oxide) (PBO), and poly(pentylene oxide) (PPeO), in order to optimize the chemical structure of the polymer-based ion transport systems. These block copolymers were selected due to their different steric hindrance and hydrophobicity, as these factors can be expected to influence both ion permeability and incorporation into membranes.

The block copolymers were synthesized via the ring-opening polymerization of γ-(2-(2-(2-methoxyethoxy)ethoxy)ethoxy) esteryl-DL-glutamate-N-carboxyanhydride (EG$_3$Glu NCA) using amine-functionalized polyether as a macroinitiator. Schemes

a Natural ion channels
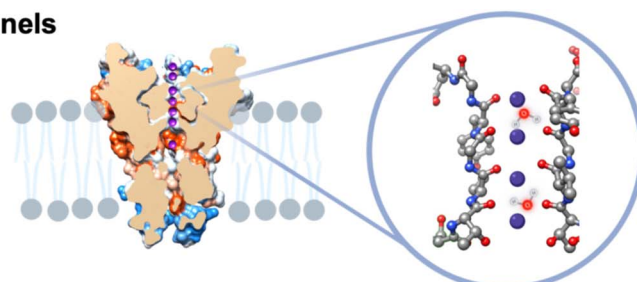
Interactions between oxygen atoms and ions, together with the presence of water in the pathway, enable cation permeation.

b Ion-permeable polymer domain

Incorporation into liposomes
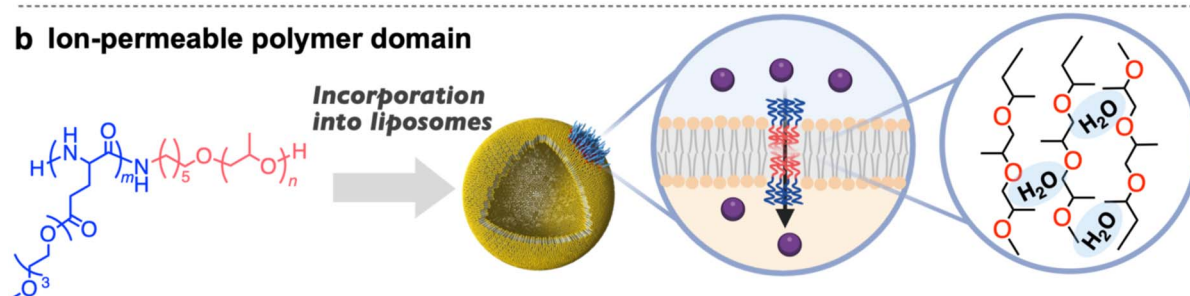
The polymer domain shows structural similarity to natural-ion-channel pathways.
✓ PPO contains ether oxygen with cation affinity
✓ The hydrophobic layer contains water

Fig. 1 (a) The ion-channel pathway in KcsA is characterized by the presence of carbonyl oxygen atoms and water molecules, which enable the transport of cations. (b) Schematic illustration of the incorporation of poly(EG$_3$Glu)-b-PPO into phospholipid bilayer membranes, which leads to the formation of polymer-rich domains. The hydrophobic core of the domains contains ether oxygen atoms and water molecules, similarly to the natural-ion-channel pathway. The domains form polymer-rich membrane region that support ion transport.
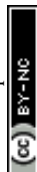
S1–S3 outline the block copolymer synthesis. Detailed synthetic procedures, representative ^{1}H NMR spectra, and size-exclusion chromatograms are provided in the SI (Fig. S1–S18).

Self-assembly of the block copolymers into vesicles and cation permeability

Poly(EG$_3$Glu)-b-PPO, which features thermoresponsive PPO as its hydrophobic segment, exhibits lower-critical-solution-temperature (LCST)-like behavior in aqueous solutions (Fig. S19).[57] To take advantage of this behavior, polymer solutions were prepared by dissolving poly(EG$_3$Glu)-b-PPO in distilled water at 0 °C in an ice bath. After full dissolution, the solution was incubated at room temperature for 30 minutes and then sonicated for 1 minute. Solutions of the other polymers, which did not exhibit LCST-like behavior, were prepared using the film-hydration method. A dynamic-light-scattering (DLS) analysis of the poly(EG$_3$Glu)-b-PPO solution showed an average hydrodynamic diameter of 151 nm with a polydispersity index (PDI) of 0.11 (Fig. 2a), and the zeta potential was −11 mV (Fig. S20). Cryo-transmission-electron-microscopy (Cryo-TEM) images revealed spherical vesicles with an average membrane thickness of ~10 nm (Fig. 2b and S21).

To obtain further structural information, we conducted small-angle-X-ray-scattering (SAXS) measurements. The SAXS profiles exhibited a q^{-2} intensity decay in the low-q region, indicating the presence of thin plate-like structures (Fig. 2c). This suggests the formation of bilayer membranes. A cross-sectional bilayer-membrane model was used to fit the SAXS data. The results indicated a hydrophilic layer thickness of 2.9 nm and a hydrophobic layer thickness of 5.5 nm to give a total membrane thickness of 11.3 nm (Table S1). These results are consistent with those of the Cryo-TEM measurements. The poly(EG$_3$Glu)-b-PPO vesicles remained stable in serum-containing culture medium (Fig. S22). The block copolymers poly(EG$_3$Glu)-b-PBO and poly(EG$_3$Glu)-b-PPeO also self-assembled into spherical vesicles as confirmed by Cryo-TEM and SAXS (Fig. S23 and S24, Tables S2 and S3).

After confirming the self-assembly of the polymers into spherical vesicles, we quantified the water content in the hydrophobic PPO layer, as water regulates ion conductance and gating in natural ion channels. For that purpose, small-angle neutron scattering (SANS) was performed (Fig. 2d). The red line in the SANS profile represents the best fit based on the cross-sectional bilayer-membrane model. The scattering-length-density (SLD) profile and structural parameters are shown in Fig. 2e and Table S4. A slight deviation at low q was observed, likely due to scattering from the overall vesicle structure, which is not captured by the bilayer cross-section model used for
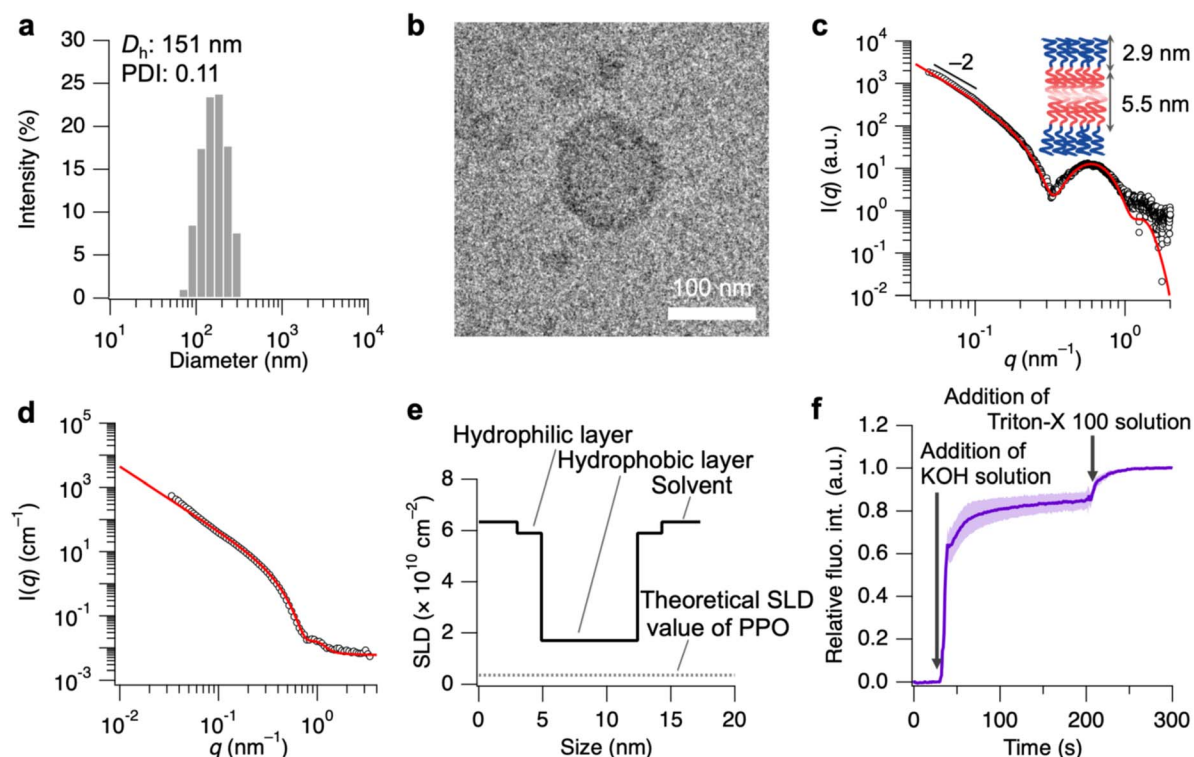

Fig. 2 (a) Size distribution of self-assembled poly(EG$_3$Glu)-b-PPO (1.0 mg mL^{-1}) in water. (b) Cryo-TEM image of a self-assembled poly(EG$_3$Glu)-b-PPO solution (10 mg mL^{-1}). (c) SAXS profile of self-assembled poly(EG$_3$Glu)-b-PPO (10 mg mL^{-1}) in water (open circles) and the theoretical curve obtained using the bilayer-membrane model (red line). (d) SANS profile of self-assembled poly(EG$_3$Glu)-b-PPO (10 mg mL^{-1}) in deuterium oxide (open circles) and the theoretical curve obtained using the bilayer-membrane model (red line). (e) SLD profile of the polymer vesicle membranes (solid line) and the theoretical SLD value of PPO (dotted line). (f) Time-dependence of the relative fluorescence intensity of HPTS encapsulated poly(EG$_3$Glu)-b-PPO vesicles upon adding KOH solution in Hepes buffer at 25 °C. The pH of the internal aqueous phase of the vesicles was 7.3, while the external aqueous phase had a pH of 7.8. [polymer] = 1 mM; [Hepes] = 10 mM. Results represent mean values ± SD (n = 3).

© 2025 The Author(s). Published by the Royal Society of Chemistry

fitting. The SLD of the hydrophobic layer (1.7×10^{10} cm^{-2}) exceeded the theoretical value for PPO (0.34×10^{10} cm^{-2}), which indicates the presence of D$_2$O in the hydrophobic region. This behavior is similar to that reported for the maltopentaose-b-PPO vesicle system.[58] The D$_2$O volume fraction in the PPO layer was calculated to be ~23 vol%.[58] Similarly, the water content in the poly(EG$_3$Glu)-b-PBO and poly(EG$_3$Glu)-b-PPeO vesicles was 16 vol% and 14 vol%, respectively (Fig. S23d and S24d, Table S4). The water content decreased with increasing length of the alkyl side chain, due to the increased steric hindrance, limiting hydrogen bonding between water molecules and the ether oxygens.

Having confirmed the hydration of the hydrophobic layer, we then evaluated the cation-transport abilities of the polymer vesicles using the pH-sensitive 8-hydroxypyrene-1,3,6-trisulfonic acid trisodium salt (HPTS) assay.[59] A solution of poly(EG$_3$Glu)-b-PPO vesicles (pH$_{inside}$ = 7.3; 10 mM Hepes) with HPTS entrapped inside the vesicles was prepared. To create a pH gradient across the polymer-bilayer membrane (pH$_{outside}$ = 7.8), KOH solution was injected into the vesicle solution. The permeation of K$^+$ ions into the polymer vesicles was monitored by measuring the change in the fluorescence intensity of the entrapped HPTS (Fig. 2f). Upon adding KOH solution, the fluorescence intensity of HPTS increased rapidly, indicating that the vesicles were permeable to K$^+$ ions. We further tested the permeability of other cation species, including divalent cations, and confirmed that all ions were able to permeate

(Fig. S25 and S26). In a similar manner, poly(EG$_3$Glu)-b-PBO and poly(EG$_3$Glu)-b-PPeO vesicles also exhibited ion permeability under the same conditions (Fig. S27). Overall, these data clearly demonstrate that all the block copolymers self-assemble into cation-permeable spherical vesicles.

Formation of polymer-rich domains in liposomes *via* block copolymer incorporation

Since spontaneous incorporation into bilayer membranes is essential for synthetic ion transport systems, we examined whether the block copolymers would spontaneously incorporate into phospholipid bilayer membranes using a post-loading method (Fig. 3a). For this purpose, we prepared liposomes (average diameter: ~100 nm) composed of 1,2-dioleoyl-sn-glycero-3-phosphocholine (DOPC) and 7-nitrobenzofurazan (NBD)-labeled 1,2-dioleoyl-sn-glycero-3-phosphoethanol amine (DOPE) and added rhodamine-labeled polymer vesicles (average diameter: ~110 nm) to the liposome solution. When poly(EG$_3$-Glu)-b-PPO vesicles were introduced, the NBD fluorescence intensity decreased, whereas the other polymer vesicles did not affect the NBD fluorescence (Fig. S28). The decrease in fluorescence was attributed to Förster resonance energy transfer (FRET), indicating that the poly(EG$_3$Glu)-b-PPO was in close proximity to the phospholipids and had spontaneously incorporated into the phospholipid bilayers. On the other hand, the lack of change in the fluorescence of NBD suggests that the
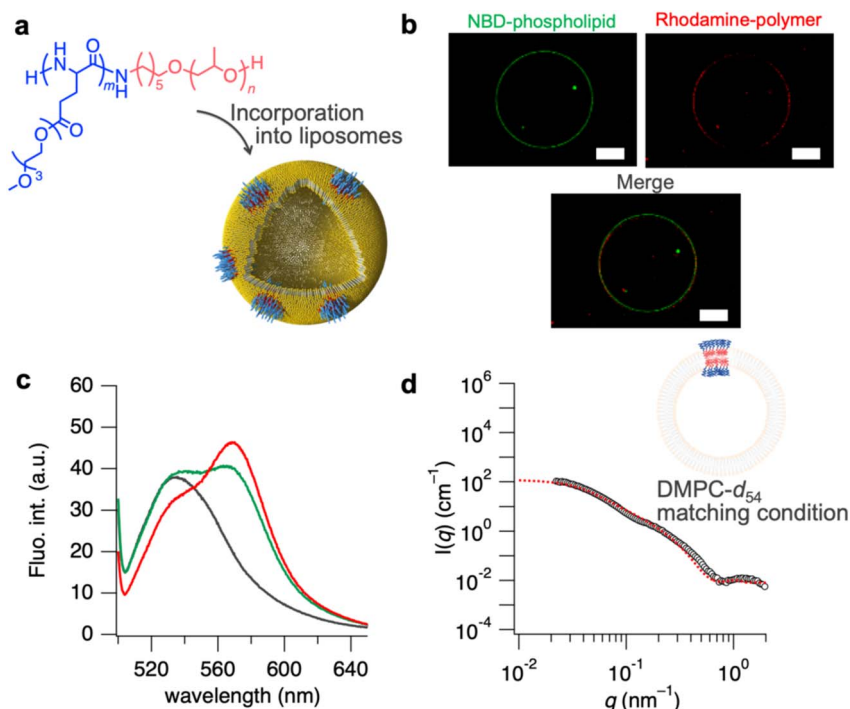

Fig. 3 (a) Schematic illustration of the incorporation of poly(EG$_3$Glu)-b-PPO into liposomes. (b) Confocal laser-scanning microscopy (CLSM) images of the polymer/phospholipid hybrid vesicles labelled with NBD-DOPE (green channel) and rhodamine-functionalized polymer (red channel); scale bar = 10 μm. (c) Fluorescence spectra of the polymer/phospholipid hybrid vesicles labeled with NBD and rhodamine (red line), polymer vesicles labeled with NBD and rhodamine (green line), and the hybrid vesicles labeled with NBD (black line). (d) SANS profile of the poly(EG$_3$Glu)-b-PPO/DMPC-d_{54} hybrid vesicles at 37 °C in 84 : 16 D$_2$O : H$_2$O (open circles) and theoretical curves obtained from the core−shell disk model (dotted red line). The 84 : 16 D$_2$O : H$_2$O ratio corresponds to the contrast-matching condition for DMPC-d_{54}.

other polymer vesicles were not incorporated into the phospholipid bilayers. The failure of these polymer vesicles to incorporate should most likely be attributed to their stability. Given that the PBO and PPeO in the polymer-bilayer membranes are less hydrated (Table S4), their membranes are stabilized by hydrophobic interactions between the hydrophobic segments. This could further inhibit the close approach and fusion of the polymer vesicles and the liposomes, thereby impeding membrane integration.

To confirm the structure of the hybrid vesicles containing poly(EG$_3$Glu)-b-PPO, we prepared micrometer-sized liposomes composed of DOPC using the film-hydration method, followed by addition of poly(EG$_3$Glu)-b-PPO vesicles (average diameter: ~110 nm) to the DOPC-giant-vesicle solutions using the post-loading method. Small amounts of rhodamine-labeled polymer and NBD-labeled DOPE were added to the polymer/phospholipid mixture to enable the polymer and phospholipid to be distinguished using confocal laser scanning microscopy (CLSM). Fig. 3b shows a representative CLSM image of polymer/DOPC vesicles containing 10 mol% of the polymer. A concentration of 10 mol% was chosen because it enables domain formation and confers molecular channel functionality, as demonstrated in our previous studies.[54,55] The colocalization of the fluorescence of rhodamine and NBD confirms the incorporation of the polymer into the DOPC membrane. Furthermore, the heterogeneous distribution of the rhodamine fluorescence within the membrane suggests the formation of polymer-rich microdomains due to the mismatch between the thickness of the polymer membrane (11.3 nm; Fig. 2c) and that of the lipid membranes (~5 nm).[48] We evaluated the membrane heterogeneity of the hybrid vesicles using another FRET analysis. The results indicated that the FRET-pair polymers were clustered on DOPC membranes, enhancing the FRET efficiency, which suggests the formation of polymer-rich heterogeneous domains in the hybrid vesicles (Fig. 3c).

To further investigate the nanostructure of the polymer-rich domains, we conducted a structural analysis of the hybrid vesicles using contrast-matching SANS. For that purpose, a mixed solution of poly(EG$_3$Glu)-b-PPO and 1,2-dimyristoyl-d_{54}-sn-glycero-3-phosphocholine (DMPC-d_{54}) was prepared with a polymer/phospholipid molar ratio of 9 : 1 by the pre-loading method. As the scattering-length density (SLD) of DMPC-d_{54} matches that of a solvent composed of 84% D$_2$O and 16% H$_2$O (Fig. S29), the phospholipids become effectively invisible, allowing structural information to be obtained solely from the polymer-rich domains.[55,60] The hybrid vesicles were analyzed in 84 vol% D$_2$O, and exhibited a SANS profile different from that of the poly(EG$_3$Glu)-b-PPO vesicles, suggesting that the scattering did not correspond to spherical vesicular structures. The SANS profile was fitted using a core–shell disk model, revealing a disk radius of 45 nm, a hydrophobic layer thickness of 4.5 nm, and an overall thickness of 9.0 nm (Fig. 3d and Table S5). The potential influence of differences between H$_2$O and D$_2$O on the membrane structure should be considered, as polymeric systems often exhibit different behaviors in these solvents due to variations in hydrogen bonding and solvation effects.[61–63] In our study, we observed a clear difference in membrane

thickness between H$_2$O and D$_2$O environments (5 nm $vs.$ 9 nm), indicating that solvent-specific interactions play a role. Although our SAXS/SANS analysis did not explicitly account for these differences, we acknowledge that they may contribute to the observed variations in membrane structure.

These results indicate that the polymer-rich phase forms disk-like bilayer structures with a polymer conformation similar to that in the bilayer membrane. Although the SANS measurements confirm the formation of disk-like polymer-rich domains, the radius of these domains (45 nm) is relatively large compared to the vesicle radius (60 nm). This may be attributed to the heterogeneous distribution of the polymer and phospholipid within each hybrid vesicle. Achieving a uniform molar ratio during the fabrication of polymer–DMPC films is challenging, and hybrid vesicles with either polymer-rich or phospholipid-rich compositions are often obtained. Consequently, the size distribution of the polymer-rich domains is broad, leading to larger domain sizes than expected.

Additionally, the SLD of the hydrophobic layer (1.0×10^{10} cm^{-2}) exceeds the theoretical SLD of PPO (0.34×10^{10} cm^{-2}), likely due to the presence of D$_2$O in the hydrophobic layer. We expected that the hydrated polymer-rich domains would facilitate ion transport.

While our analysis indicates the formation of polymer-rich domains within hybrid vesicles, we acknowledge that a single, well-defined domain type may not prevail at the polymer concentrations used in this study. Previous studies have reported alternative morphologies—including interconnected or "parachute"-like structures—particularly under conditions of hydrophobic mismatch between polymer and lipid components.[64–66] Our previous studies demonstrated that this class of block copolymers can induce domain formation at 10 mol% in lipid membranes,[54,55] and the present FRET, SANS, and CLSM results further support the formation of polymer-rich domains.

However, it should be noted that the core–shell disk model used for fitting the SANS data does not explicitly account for domain curvature or structural heterogeneity. The presence of multiple domain morphologies and partial polymer incorporation may lead to variations in local curvature and scattering length density, which are not fully captured by the current model. These structural features may explain the slight deviations observed between the experimental and fitted SANS profiles. The possible presence of structurally heterogeneous or partially continuous domains may also contribute to variability in ion permeability and should be considered in future work.

Ion transport facilitated by polymer-rich domains in liposomes

After successfully achieving the incorporation of poly(EG$_3$Glu)-b-PPO into liposomes and the formation of the polymer-rich domains, we shifted our focus to exploring the potential of these domains to facilitate cation transport in liposomal membranes. We prepared a solution of DOPC liposomes (pH$_{inside}$ = 7.3; 10 mM Hepes) with encapsulated HPTS. A pH gradient (pH$_{outside}$ = 7.8) was created by injecting KOH solution
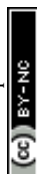
into the liposome solution, and poly(EG$_3$Glu)-b-PPO was then added to give a DOPC-to-polymer molar ratio of 9 : 1(Fig. 4a). After adding the polymer, the fluorescence intensity of HPTS increased with time, indicating that K$^+$ transport across the liposomal membrane was facilitated by the formation of the polymer domains (Fig. 4b). As the poly(EG$_3$Glu)-b-PBO and poly(EG$_3$Glu)-b-PPeO vesicles could not be integrated into liposomes via the post-loading method, no increase in fluorescence intensity was observed when they were added to the HPTS-loaded DOPC liposome solution (Fig. S30).

To obtain further insight into the ion transport activity, the EC$_{50}$ value (the concentration required to reach half the maximum activity) was determined to be 27 μM (2.7 mol%), and the Hill coefficient n was calculated to be ∼0.6, indicating negative cooperativity (Fig. S31). The Hill equation is commonly used to assess the relationship between ligand concentration and biological or physicochemical responses. The Hill coefficient provides a measure of apparent cooperativity, where $n > 1$ indicates positive cooperativity, $n = 1$ indicates non-cooperative (independent) behavior, and $n < 1$ suggests negative cooperativity or functional heterogeneity. A possible explanation for the negative-cooperativity Hill coefficient is that each polymer may transport two K$^+$ ions simultaneously. Additionally, the entry of hydrated K$^+$ ions into the hydrophobic region of the domain

could increase the local water content, leading to negative cooperativity. Based on the observed K$^+$ ion transport activity of the polymer domain, we also investigated the cation selectivity. The polymer domains showed a weak selectivity for Rb$^+$ ions over other alkaline ions, following the order Rb$^+$ > K$^+$ > Cs$^+$ > Na$^+$ > Li$^+$, in accordance with the Eisenman sequence III (Fig. 4c and S32).[67] Cation selectivity is generally determined by the affinity of a channel for specific cations and the magnitude of the cation dehydration energy. In our case, the polymer domains lack sufficient affinity for specific cations, resulting in low cation selectivity. Further research is required to understand how the molecular design of ion permeable polymer domains could be optimized to enhance cation affinity. To further determine the transport mechanism of the ion permeable polymer domains, we performed HPTS assays in the presence of the proton carrier cyanide-4-(trifluoromethoxy)phenylhydrazone (FCCP) or the K$^+$ carrier valinomycin. In the presence of FCCP, the hybrid vesicles showed a drastic increase in HPTS fluorescence (Fig. S33), whereas valinomycin did not significantly increase the fluorescence intensity (Fig. S34), suggesting that the polymer domains act as M$^+$/H$^+$ antiporters, in which M$^+$ is transported more rapidly than H$^+$.

To extend our understanding of the ion transport activity of poly(EG$_3$Glu)-b-PPO, the ionic conductance across the planar
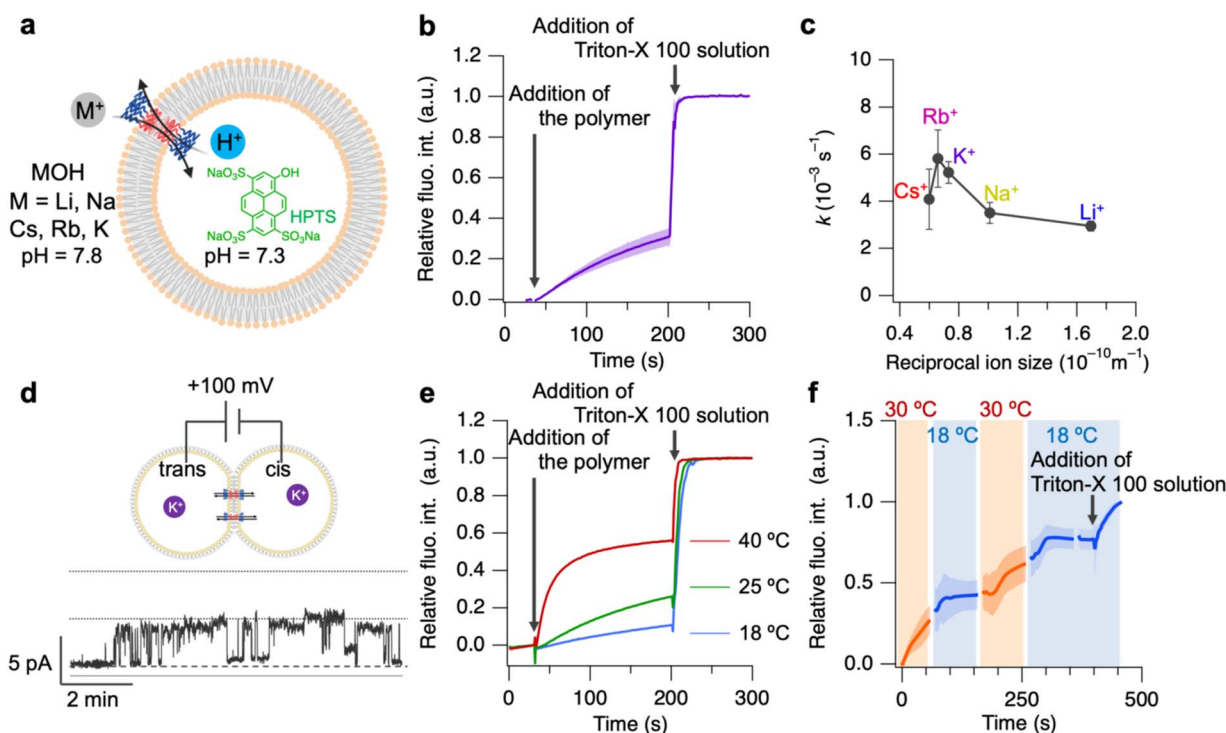

Fig. 4 (a) Schematic illustration of the HPTS assay used to measure the ion-transport activity of the polymer domains in the DOPC liposomes (pH$_{inside}$ = 7.3; pH$_{outside}$ = 7.8). (b) Time-dependent changes in the relative fluorescence intensity of encapsulated HPTS following the addition of poly(EG$_3$Glu)-b-PPO vesicles. [DOPC] = 0.9 mM, [polymer] = 0.1 mM. Results represent mean values ± SD (n = 3). (c) Pseudo-first-order rate constants as a function of the reciprocal cation size, as determined via the HPTS assay. (d) Representative channel-current traces of the polymer domain recorded in symmetric solutions (cis chamber = 1 M KCl; $trans$ chamber = 1 M KCl). No membrane leakage was observed in the DPhPC membranes without the polymer, as demonstrated by the current signal at +100 mV (Fig. S36). (e) Solution-temperature-dependent potassium-ion permeability of the polymer domain. (f) Reversible changes in the potassium-ion permeability of the domain with temperature variation. Results represent mean values ± SD (n = 3).

bilayer membrane was examined. Two compartments (*cis* and *trans* chambers) containing KCl solution were separated by a planar lipid-bilayer membrane composed of diphytanoyl phosphatidylcholine (DPhC). The single-channel current signals were detected with both open and closed states (Fig. 4d). Such transitions have been reported in natural/artificial ion channels,[23,68,69] and the channel conductance was found to be 53 ± 11 pS, which is similar to the conductance of an artificial ion channel with a diameter of ~0.6 nm.[23] These results suggest that this polymer may adopt a channel-like configuration. In addition to the channel signals, erratic signals were observed, suggesting detergent-like behavior (Fig. S35).[70] These erratic current fluctuations might be caused due to the amphiphilic properties of the polymer.

We also performed HPTS assays using salts with different counter anions, including NaCl, NaBr, and NaI. The fluorescence responses were nearly identical (Fig. S37), indicating that the polymer domains permit anion permeation but do not strongly discriminate among halide anions under these conditions. Consistently, lucigenin-based assays indicated a moderate level of chloride transport. (Fig. S38). These results support the conclusion that the polymer domains enable ion transport, allowing the passage of both cations and anions.

A key characteristic of the hydrophobic layer in the polymer domains is its weak hydration, and our previous study demonstrated that the degree of hydration can be controlled by adjusting the temperature.[58] Given that hydration affects cation permeation, we anticipated that the permeation rate could be tuned by changing the solution temperature. As shown in Fig. 4e, the fluorescence intensity hardly increased after the addition of the polymer at 18 °C, whereas the permeation rate increased with increasing temperature. This suggests that at lower temperatures, the higher degree of hydration inhibits ion dehydration, thus suppressing permeation (Fig. S39 and Table S6). In contrast, as the temperature rises, the reduced hydration facilitates ion dehydration and thus enhances the permeation rate. Furthermore, an HPTS assay of the hybrid vesicles under alternating temperatures of 30 °C and 18 °C was performed. The results demonstrate that cation permeation can be switched on and off, *i.e.*, the vesicles are impermeable at 18 °C and permeable at 30 °C (Fig. 4f). These findings indicate that cation permeation can be regulated by controlling the degree of hydration. To further elucidate the role of water in this process, changing the H_2O/D_2O composition could provide deeper insights into its influence within the transport pathways composed of PPO. This aspect remains an important subject for future investigations. Overall, these data clearly demonstrate that the polymer domains facilitate thermoresponsive ion transport across lipid membranes.

Block copolymer-mediated ion transport Perturbs ion homeostasis and induces apoptosis in cancer cells

After demonstrating that the polymer facilitates ion transport in liposomal membranes, we next investigated whether it could mediate similar activity in biological membranes. We hypothesized that the incorporation of the block copolymer into cell membranes would disrupt ion homeostasis, thereby triggering apoptosis *via* activation of the intrinsic apoptotic pathway. Thus, we first confirmed the incorporation of the polymer into cell membranes using membrane-staining techniques. Rhodamine-labeled polymer vesicles were added to the culture medium of murine colorectal carcinoma (CT26) cells. Intracellular rhodamine fluorescence was observed after 1 h of incubation, indicating the successful incorporation of the polymer into the cells (Fig. S40). These results were further corroborated by flow cytometry (Fig. S41). Notably, co-localization of the rhodamine signal with the cell membrane staining dye Plas-Mem Bright Green confirmed that the polymer had been incorporated into the cell membrane (Fig. 5a).

Next, to determine whether the incorporated polymer still functions as a cation permeable domain, we examined changes in intracellular K^+ concentration using the indicator Potassium Green-2 AM. The intracellular K^+ concentration gradually decreased with increasing incubation time (Fig. 5b). These results clearly demonstrate that the block copolymer domains support cation permeability in living cells. Furthermore, the live–dead assay revealed that the cancer cells underwent cell death in response to these intracellular ion concentration changes (Fig. 5c). The IC_{50} value (the concentration required to inhibit 50% of cell viability) was determined to be ~20 μM using the LDH assay (Fig. S42).

Dysregulation of ion homeostasis is frequently associated with activation of the intrinsic apoptotic pathway.[71,72] To assess whether cell death was induced by apoptosis, CT26 cells were incubated with poly(EG_3Glu)-*b*-PPO for 24 h, followed by treatment with fluorescein-annexin V and propidium iodide (PI). Cells exposed to the polymer showed positive annexin V binding and PI uptake, with 11% of cells in early apoptosis and 41% in late apoptosis (Fig. 5d).

During the early stage of apoptosis, the loss of mitochondrial membrane potential (MMP) occurs.[21,73,74] MMP changes were evaluated in CT26 cells using the membrane-potential-sensitive dye JC-1, which exhibits red fluorescence emission due to the formation of J-aggregates in healthy mitochondrial membranes. MMP depolarization leads to dispersion of these aggregates, resulting in green fluorescence.[75,76] CT26 cells treated with the polymer vesicles showed a significant decrease in red fluorescence and a concurrent increase in green fluorescence with prolonged incubation (Fig. S43). Our results thus suggest that the incorporation of the block copolymer into the cell membrane enhances MMP depolarization.

MMP perturbation has been linked with increased oxidative stress and the production of reactive oxygen species (ROS).[77,78] The cells treated with the polymer exhibited elevated ROS levels, as evident from the increased green fluorescence of the ROS-sensitive probe DCFH-DA (Fig. S44). The rise in intracellular ROS facilitates the opening of the mitochondrial permeability transition pores, leading to the release of cytochrome c from the mitochondria into cytoplasm,[79] which in turn activates caspase-9 and caspase-3 expression. We thus examined the expression of the caspase family to better understand the pathway of mitochondria-dependent apoptosis. An immunoblotting analysis revealed decreased levels of both caspase-9 and caspase-3
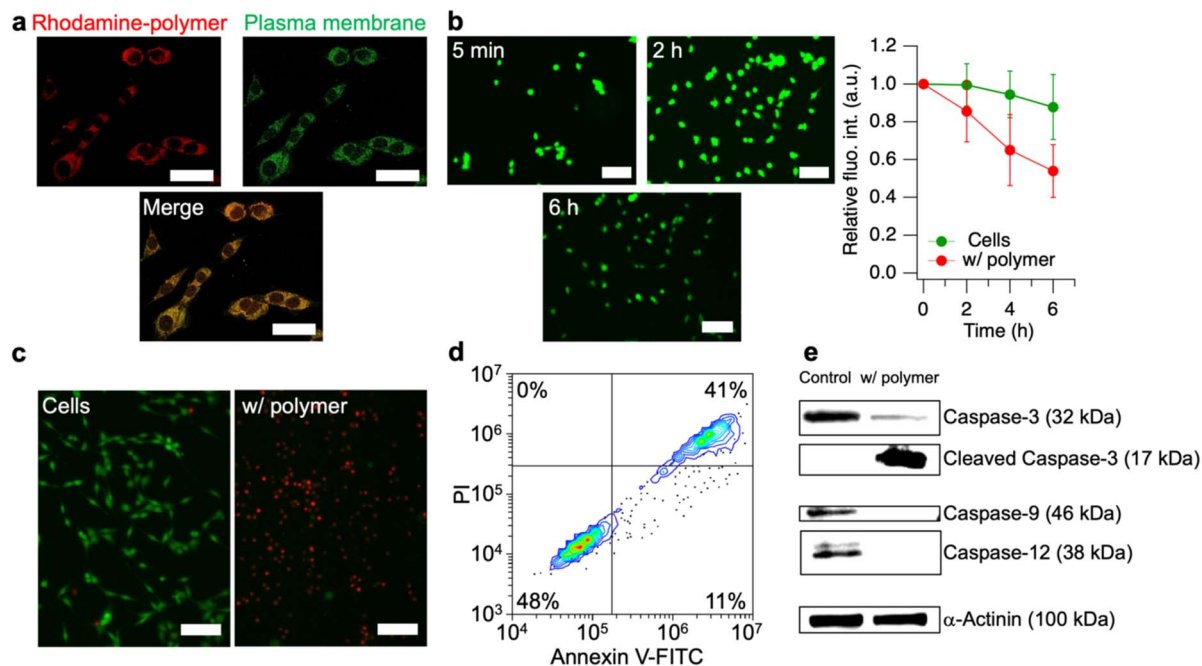
Fig. 5 (a) CLSM images of CT26 cells incubated for 6 h with rhodamine-labeled poly(EG$_3$Glu)-*b*-PPO, followed by staining of the plasma membrane with PlasMem Bright Green; scale bar = 50 μm. (b) Fluorescence images showing changes in the potassium-ion concentrations in CT26 cells treated with poly(EG$_3$Glu)-*b*-PPO (left), and a quantitative comparison of the relative fluorescence intensity between untreated CT26 cells and those treated with poly(EG$_3$Glu)-*b*-PPO (right); scale bar = 50 μm. (c) Representative fluorescence images of CT26 cells following live/dead staining after treatment with or without poly(EG$_3$Glu)-*b*-PPO; scale bar = 100 μm. (d) Flow cytometry analysis of CT26 cells treated with poly(EG$_3$Glu)-*b*-PPO for 24 h and stained with FITC-Annexin V and PI to evaluate apoptosis. (e) Western-blot analysis of apoptosis-related proteins (caspase-3, cleaved caspase-3, caspase-9, caspase-12) with α-actinin as a control.

following co-incubation with poly(EG$_3$Glu)-*b*-PPO (Fig. 5e). Notably, cleaved caspase-3, a hallmark of apoptosis, was also observed. Furthermore, the reduced expression of caspase-12 suggests an involvement of apoptosis mediated by endoplasmic-reticulum stress.[38,80] Collectively, the decreased expression of caspase-3, caspase-9, and caspase-12, in combination with the appearance of cleaved caspase-3, clearly indicates that the apoptotic cell death induced by the block copolymers occurs *via* the caspase-mediated intrinsic pathway. Although our data indicate that cation transport contributes to apoptosis, the observed anion permeability suggests that anion transport may also play a role in disrupting ion homeostasis and triggering apoptotic signaling.[74,81]

Evaluation of antitumor effects using block copolymer vesicles in tumor-bearing mice

The ion transport ability of the block copolymer domains to induce cancer-cell apoptosis prompted us to evaluate their antitumor activity *in vivo* (Fig. 6a). Although the polymers exhibit ion transport activity, they lack tumor-cell selectivity. To improve tumor-cell targeting, we synthesized folic-acid-functionalized poly(EG$_3$Glu)-*b*-PPO, as folic-acid receptors are overexpressed on the surface of many cancer cells.[82,83] Co-assembly of 10 mol% folic-acid-functionalized polymer with poly(EG$_3$Glu)-*b*-PPO successfully yielded folic-acid-presenting polymer vesicles, whose IC$_{50}$ value (20 μM) against CT26 cells was comparable to that of the poly(EG$_3$Glu)-*b*-PPO vesicles

(Fig. S45). However, the IC$_{50}$ value remains higher than that of the clinically used anticancer drug doxorubicin (0.9 μM), indicating that further structural optimization is required to enhance potency. Additionally, cytotoxicity was evaluated using HEK293 cells as a model for normal cells, and the polymer vesicles exhibited similar IC$_{50}$ values (15 μM) compared to CT26 cells (Fig. S46). These results suggest that, although the polymer vesicles are less potent than doxorubicin, they do not show significant selectivity between cancer and normal cells, indicating the need for further modification to improve cancer cell specificity.

Prior to assessing the antitumor activity, we investigated the pharmacokinetic profiles and organ distribution of the folic-acid-presenting polymer vesicles in BALB/c mice with CT26 tumors. Rhodamine-labeled, folic-acid-presenting polymer vesicles (5 mg mL^{-1}, 0.1 mL) were intravenously injected into the tail vein, and blood samples were collected at pre-determined intervals (1, 2, 4, 8, 24, and 48 h) to monitor blood clearance. The rhodamine fluorescence of the blood samples indicated that approximately 14% of the injected dose remained 4 h after injection, suggesting that the vesicles distribute rapidly to specific tissues during circulation (Fig. 6b). To evaluate bi-odistribution, the mice were euthanized 24 or 48 h after injection of the vesicle solutions, and various organs and tissues, including heart, lung, spleen, liver, kidney, and tumor, and blood were collected and homogenized. The fluorescence intensity of the supernatants was measured (Fig. 6c), and the
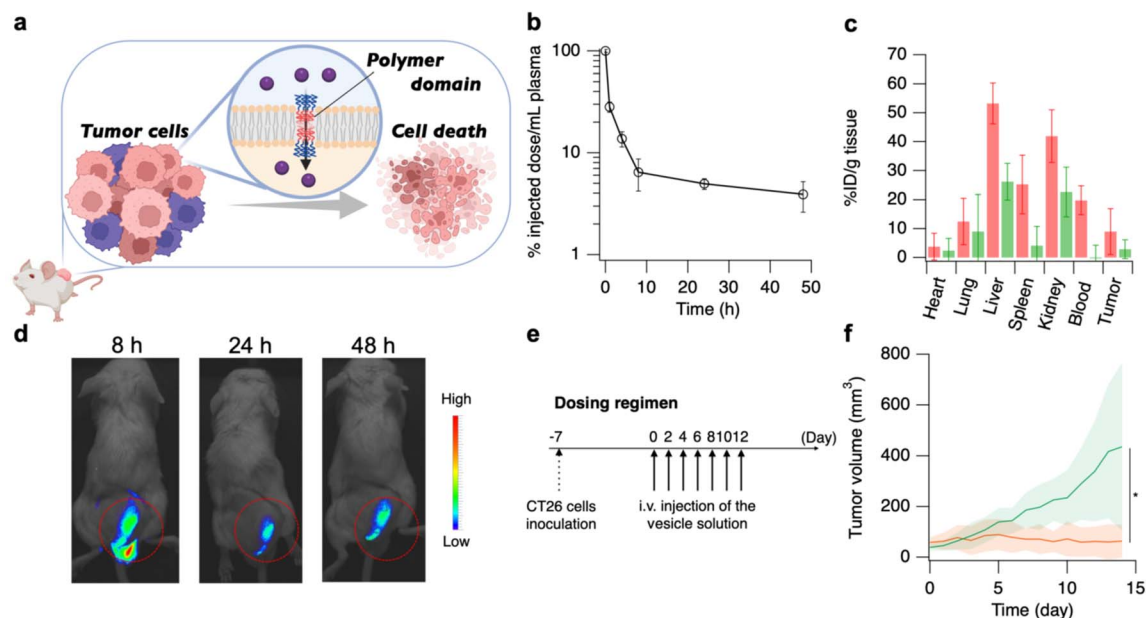
Fig. 6 (a) Schematic illustration of ion transport across the cancer cell membrane mediated by polymer domains at the tumor site. (b) Changes in plasma concentrations of polymer vesicles in mice over time; results represent mean values ± SD ($n = 6$). (c) Biodistribution of the rhodamine-labelled, folic-acid-presenting polymer vesicles at 24 (red bars) and 48 h (green bars) after intravenous injection; results represent mean values ± SD ($n = 6$). (d) Near infrared fluorescence images of CT26 tumor-bearing mice after intravenous injection of NIR 797-labelled, folic-acid-presenting polymer vesicles via the tail vain. Red circle indicates location of the tumor. (e) Dosing regimen used in the antitumor-activity study. (f) Tumor growth over a 14 day period following the different treatments. Mice treated with intravenous (i.v.) injection of PBS buffer (green line) and mice treated with i.v. injection of the folic-acid-presenting polymer vesicles (red line); results represent mean values ± SD ($n = 5$). Statistical significance was determined using the Mann–Whitney U test (*$P < 0.05$; actual $P = 0.017$).

vesicles were found to mainly accumulate in the reticuloendothelial system (liver and spleen) and the kidney. Notably, the tumor accumulation reached approximately 10% ID/g, which exceeds typical levels attributed to the EPR effect alone.[84] *In vivo* fluorescence imaging revealed that the vesicles rapidly accumulated in the tumor and remained there for an extended period (Fig. 6d). This enhanced accumulation is likely due, at least in part, to active targeting mediated by the folate ligands on the polymer vesicle surface. Although significant accumulation was observed in the tumor, relatively high fluorescence signals were also detected in the lung and blood. The accumulation in the lung is likely due to mechanical trapping of the relatively large vesicles within the narrow capillary network, a phenomenon commonly reported for nanoparticles with limited deformability. The presence in blood suggests prolonged circulation, which may enhance tumor access over time but also underscores the need for further optimization to improve targeting specificity and reduce off-target distribution.

Having confirmed the tumor accumulation of the polymer vesicles, we then evaluated the antitumor activity of the folic-acid-presenting vesicles in CT26-tumor-bearing mice. For this purpose, vesicle solutions were injected intravenously every 2 days for a total of seven administrations (Fig. 6e). As shown in Fig. 6f, the mice treated with the polymer-vesicle solution exhibited complete suppression of tumor growth, whereas the tumors progressed in the PBS-treated group (Fig. S47). Importantly, the mice treated with the vesicles did not show significant body-weight loss (Fig. S48), indicating that no serious systemic toxicity arose from the use of the polymer vesicles. Additionally, the urea nitrogen (UN), alanine aminotransferase (ALT), and alkaline phosphatase (ALP) levels of the mice were evaluated to monitor potential liver and kidney toxicity (Fig. S49). The observed UN, ALT, and ALP levels were comparable to those of PBS-treated mice, indicating that treatment with the polymer vesicles did not induce hepatotoxicity or nephrotoxicity. In their entirety, these findings demonstrate that poly(EG$_3$Glu)-*b*-PPO block copolymers, by mediating ion transport across cellular membranes, hold promise as a novel and potentially safe therapeutic platform for cancer treatment.

Conclusions

In summary, we developed thermoresponsive poly(EG$_3$Glu)-conjugated poly(propylene oxide) block copolymers that self-assemble into vesicles and spontaneously integrate into biological membranes to form polymer-rich domains. These domains facilitate ion transport, by creating hydrated microenvironments within the membrane, thereby contributing to intracellular ion flux. The resulting disruption of ion homeostasis is associated with apoptotic responses in cancer cells. Notably, when administered intravenously, the vesicles accumulated in tumors and led to significant tumor growth inhibition.

These polymers exhibit several advantages over conventional ion channels. First, their macromolecular and supramolecular nature reduces their susceptibility to renal clearance and

enables tumor accumulation *via* the EPR effect. Second, these polymer assemblies do not require specific secondary structures such as helices[13,85] or pores,[86,87] thus facilitating more straightforward and versatile design.

Further investigations revealed important properties of these block copolymers when incorporated into lipid membranes. Specifically, although poly(EG$_3$Glu)-*b*-PBO and poly(EG$_3$Glu)-*b*-PPeO did not spontaneously incorporate into biological membranes, they were integrated into lipid membranes through pre-loading with phospholipids to form vesicles (Fig. S50 and S51). The polymer domains formed in this manner exhibit faster K$^+$ transport compared to poly(EG$_3$Glu)-*b*-PPO polymer domains (Fig. S52). All hybrid vesicles were prepared using the same pre-loading method; thus, the observed differences in ion transport are likely attributable to the chemical nature of the block copolymers rather than the preparation method. These results suggest that modulation of hydration within the hydrophobic membrane region can serve as a tunable parameter for controlling ion transport properties—an avenue under investigation.

Together, these results highlight membrane-integrated, ion-permeable polymer domains as a robust and adaptable platform for engineering synthetic ion transport systems. Beyond cancer therapy, this approach may be extended to treat diseases linked to dysregulated ion homeostasis, such as liver fibrosis and cardiovascular disorders,[88,89] or to design functional biointerfaces and next-generation stimuli-responsive materials.

Author contributions

All authors have given approval to the final version of this manuscript.

Conflicts of interest

There are no conflicts to declare.

Data availability

The data supporting this article have been included as part of the SI.

The SI file contains experimental procedures, characterization data, and supporting figures and tables. See DOI: **https://doi.org/10.1039/d5sc04256a**.

Acknowledgements

Notes and references

1 J. Ackerman Michael and E. Clapham David, *N. Engl. J. Med.*, 1997, **336**, 1575–1586.

2 I. Tabushi, Y. Kuroda and K. Yokota, *Tetrahedron Lett.*, 1982, **23**, 4601–4604.

3 T. M. Fyles, *Chem. Soc. Rev.*, 2007, **36**, 335–347.

4 G. W. Gokel and S. Negin, *Acc. Chem. Res.*, 2013, **46**, 2824–2833.

5 N. Sakai and S. Matile, *Langmuir*, 2013, **29**, 9031–9040.

6 S.-P. Zheng, L.-B. Huang, Z. Sun and M. Barboiu, *Angew. Chem., Int. Ed.*, 2021, **60**, 566–597.

7 K. Sato, T. Muraoka and K. Kinbara, *Acc. Chem. Res.*, 2021, **54**, 3700–3709.

8 X. Yuan, J. Shen and H. Zeng, *Chem. Commun.*, 2024, **60**, 482–500.

9 S. Qi, C. Zhang, H. Yu, J. Zhang, T. Yan, Z. Lin, B. Yang and Z. Dong, *J. Am. Chem. Soc.*, 2021, **143**, 3284–3288.

10 L. Zhang, J. Tian, Z. Lin and Z. Dong, *J. Am. Chem. Soc.*, 2024, **146**, 8500–8507.

11 F. Chen, J. Shen, N. Li, A. Roy, R. Ye, C. Ren and H. Zeng, *Angew. Chem., Int. Ed.*, 2020, **59**, 1440–1444.

12 W.-L. Huang, X.-D. Wang, Y.-F. Ao, Q.-Q. Wang and D.-X. Wang, *Angew. Chem., Int. Ed.*, 2023, **62**, e202302198.

13 C. Lang, W. Li, Z. Dong, X. Zhang, F. Yang, B. Yang, X. Deng, C. Zhang, J. Xu and J. Liu, *Angew. Chem., Int. Ed.*, 2016, **55**, 9723–9727.

14 L. Cao, I. C. Chen, Z. Li, X. Liu, M. Mubashir, R. A. Nuaimi and Z. Lai, *Nat. Commun.*, 2022, **13**, 7894.

15 S. Deng, Z. Li, L. Yuan, J. Shen and H. Zeng, *Nano Lett.*, 2024, **24**, 10750–10758.

16 K. Sato, R. Sasaki, R. Matsuda, M. Nakagawa, T. Ekimoto, T. Yamane, M. Ikeguchi, K. V. Tabata, H. Noji and K. Kinbara, *J. Am. Chem. Soc.*, 2022, **144**, 11802–11809.

17 R. Sasaki, K. Sato, K. V. Tabata, H. Noji and K. Kinbara, *J. Am. Chem. Soc.*, 2021, **143**, 1348–1355.

18 T. Muraoka, D. Noguchi, R. S. Kasai, K. Sato, R. Sasaki, K. V. Tabata, T. Ekimoto, M. Ikeguchi, K. Kamagata, N. Hoshino, H. Noji, T. Akutagawa, K. Ichimura and K. Kinbara, *Nat. Commun.*, 2020, **11**, 2924.

19 T. Muraoka, K. Umetsu, K. V. Tabata, T. Hamada, H. Noji, T. Yamashita and K. Kinbara, *J. Am. Chem. Soc.*, 2017, **139**, 18016–18023.

20 T. Muraoka, T. Endo, K. V. Tabata, H. Noji, S. Nagatoishi, K. Tsumoto, R. Li and K. Kinbara, *J. Am. Chem. Soc.*, 2014, **136**, 15584–15595.

21 H. Yang, J. Yi, S. Pang, K. Ye, Z. Ye, Q. Duan, Z. Yan, C. Lian, Y. Yang, L. Zhu, D.-H. Qu and C. Bao, *Angew. Chem., Int. Ed.*, 2022, **61**, e202204605.

22 W.-Z. Wang, L.-B. Huang, S.-P. Zheng, E. Moulin, O. Gavat, M. Barboiu and N. Giuseppone, *J. Am. Chem. Soc.*, 2021, **143**, 15653–15660.

23 R. Kawano, N. Horike, Y. Hijikata, M. Kondo, A. Carné-Sánchez, P. Larpent, S. Ikemura, T. Osaki, K. Kamiya, S. Kitagawa, S. Takeuchi and S. Furukawa, *Chem*, 2017, **2**, 393–403.

24 R. Paul, D. Dutta, T. K. Mukhopadhyay, D. Müller, B. Lala, A. Datta, H. Schwalbe and J. Dash, *Nat. Commun.*, 2024, **15**, 5275.

25 Z. Chen, X. Xie, C. Jia, Q. Zhong, Q. Zhang, D. Luo, Y. Cao, Y. Mu and C. Ren, *Angew. Chem., Int. Ed.*, 2024, **63**, e202318811.

26 Y. Wu, C. Li, Y. Wu, J. Xu, Z. Ni, O. Reany, T. Yan, D. Zhu and J. Liu, *Adv. Funct. Mater.*, 2024, **34**, 2400432.

27 Q. Zhong, Y. Cao, X. Xie, Y. Wu, Z. Chen, Q. Zhang, C. Jia, Z. Wu, P. Xin, X. Yan, Z. Zeng and C. Ren, *Angew. Chem., Int. Ed.*, 2024, **63**, e202314666.

28 J. Yang, G. Yu, J. L. Sessler, I. Shin, P. A. Gale and F. Huang, *Chem*, 2021, **7**, 3256–3291.

29 S.-H. Park, I. Hwang, D. A. McNaughton, A. J. Kinross, E. N. W. Howe, Q. He, S. Xiong, M. D. Kilde, V. M. Lynch, P. A. Gale, J. L. Sessler and I. Shin, *Chem*, 2021, **7**, 3325–3339.

30 T. Saha, A. Gautam, A. Mukherjee, M. Lahiri and P. Talukdar, *J. Am. Chem. Soc.*, 2016, **138**, 16443–16451.

31 J. A. Malla, R. M. Umesh, A. Vijay, A. Mukherjee, M. Lahiri and P. Talukdar, *Chem. Sci.*, 2020, **11**, 2420–2428.

32 J. Shi, P. W. Kantoff, R. Wooster and O. C. Farokhzad, *Nat. Rev. Cancer*, 2017, **17**, 20–37.

33 M. J. Ernsting, M. Murakami, A. Roy and S.-D. Li, *J. Controlled Release*, 2013, **172**, 782–794.

34 N. Bertrand and J.-C. Leroux, *J. Controlled Release*, 2012, **161**, 152–163.

35 Y. Lin, B. Wu, Y. Zeng, H. Yuan, C. Ji, Z. Liu, Y. Sui, T. Yin, X. Kong, Y. Zhu, J. Chen and C. Lang, *Angew. Chem., Int. Ed.*, 2024, **63**, e202408558.

36 T. Yan, S. Liu, C. Li, J. Xu, S. Yu, T. Wang, H. Sun and J. Liu, *Angew. Chem., Int. Ed.*, 2022, **61**, e202210214.

37 C. Li, Y. Wu, Y. Zhu, J. Yan, S. Liu, J. Xu, S. Fa, T. Yan, D. Zhu, Y. Yan and J. Liu, *Adv. Mater.*, 2024, **36**, 2312352.

38 D. Lee, S.-H. Lee, I. Noh, E. Oh, H. Ryu, J. Ha, S. Jeong, J. Yoo, T.-J. Jeon, C.-O. Yun and Y.-C. Kim, *Adv. Sci.*, 2019, **6**, 1801995.

39 S. Liu, W. Xu, J. Zheng, K. Ngocho, H. Chen, K. Wang, S. Xiong, X. He and J. Liu, *Adv. Healthcare Mater.*, 2024, **13**, 2402023.

40 T. Jiang, A. Hall, M. Eres, Z. Hemmatian, B. Qiao, Y. Zhou, Z. Ruan, A. D. Couse, W. T. Heller, H. Huang, M. O. de la Cruz, M. Rolandi and T. Xu, *Nature*, 2020, **577**, 216–220.

41 M. Schulz and W. H. Binder, *Macromol. Rapid Commun.*, 2015, **36**, 2031–2041.

42 J. Y. Kang, I. Choi, M. Seo, J. Y. Lee, S. Hong, G. Gong, S. S. Shin, Y. Lee and J. W. Kim, *J. Colloid Interface Sci.*, 2020, **561**, 318–326.

43 Y. K. Go, N. Kambar and C. Leal, *Polymers*, 2020, **12**(6), 1232.

44 M. Schulz, D. Glatte, A. Meister, P. Scholtysek, A. Kerth, A. Blume, K. Bacia and W. H. Binder, *Soft Matter*, 2011, **7**, 8100–8110.

45 J. F. Le Meins, C. Schatz, S. Lecommandoux and O. Sandre, *Mater. Today*, 2013, **16**, 397–402.

46 M. Chemin, P.-M. Brun, S. Lecommandoux, O. Sandre and J.-F. Le Meins, *Soft Matter*, 2012, **8**, 2867–2874.

47 T. P. T. Dao, A. Brûlet, F. Fernandes, M. Er-Rafik, K. Ferji, R. Schweins, J. P. Chapel, A. Fedorov, M. Schmutz, M. Prieto, O. Sandre and J. F. Le Meins, *Langmuir*, 2017, **33**, 1705–1715.

48 Y. K. Go and C. Leal, *Chem. Rev.*, 2021, **121**, 13996–14030.

49 T. Hoomann, N. Jahnke, A. Horner, S. Keller and P. Pohl, *Proc. Natl. Acad. Sci. U. S. A.*, 2013, **110**, 10842–10847.

50 H. T. Kratochvil, J. K. Carr, K. Matulef, A. W. Annen, H. Li, M. Maj, J. Ostmeyer, A. L. Serrano, H. Raghuraman, S. D. Moran, J. L. Skinner, E. Perozo, B. Roux, F. I. Valiyaveetil and M. T. Zanni, *Science*, 2016, **353**, 1040–1044.

51 C. I. Lynch, S. Rao and M. S. P. Sansom, *Chem. Rev.*, 2020, **120**, 10298–10335.

52 M. J. Ryan, L. Gao, F. I. Valiyaveetil, A. A. Kananenka and M. T. Zanni, *J. Am. Chem. Soc.*, 2024, **146**, 1543–1553.

53 T. Nishimura, Y. Sasaki and K. Akiyoshi, *Adv. Mater.*, 2017, **29**, 1702406.

54 T. Nishimura, S. Hirose, Y. Sasaki and K. Akiyoshi, *J. Am. Chem. Soc.*, 2020, **142**, 154–161.

55 N. Ozawa, S. Kosaka, S. Fujii and T. Nishimura, *Polym. Chem.*, 2023, **14**, 2198–2204.

56 W. F. Paxton, P. T. McAninch, K. E. Achyuthan, S. H. R. Shin and H. L. Monteith, *Colloids Surf., B*, 2017, **159**, 268–276.

57 D. Roy, W. L. A. Brooks and B. S. Sumerlin, *Chem. Soc. Rev.*, 2013, **42**, 7214–7243.

58 T. Nishimura, L. de Campo, H. Iwase and K. Akiyoshi, *Macromolecules*, 2020, **53**, 7546–7551.

59 N. Sakai and S. Matile, *J. Phys. Org. Chem.*, 2006, **19**, 452–460.

60 V. K. Sharma, E. Mamontov, M. Tyagi, S. Qian, D. K. Rai and V. S. Urban, *J. Phys. Chem. Lett.*, 2016, **7**, 2394–2401.

61 C. Liang, A. Rayabharam and N. R. Aluru, *J. Phys. Chem. B*, 2023, **127**, 6532–6542.

62 L. P. Kreuzer, T. Widmann, N. Hohn, K. Wang, L. Bießmann, L. Peis, J.-F. Moulin, V. Hildebrand, A. Laschewsky, C. M. Papadakis and P. Müller-Buschbaum, *Macromolecules*, 2019, **52**, 3486–3498.

63 G. Giubertoni, M. Bonn and S. Woutersen, *J. Phys. Chem. B*, 2023, **127**, 8086–8094.

64 J. F. Tallman, N. Kambar, C. Leal and A. Statt, *Macromolecules*, 2024, **57**, 11688–11696.

65 M. Jung, D. H. W. Hubert, P. H. H. Bomans, P. M. Frederik, J. Meuldijk, A. M. van Herk, H. Fischer and A. L. German, *Langmuir*, 1997, **13**, 6877–6880.

66 M. Jung, D. H. W. Hubert, E. van Veldhoven, P. Frederik, A. M. van Herk and A. L. German, *Langmuir*, 2000, **16**, 3165–3174.

67 G. Eisenman and R. Horn, *J. Membr. Biol.*, 1983, **76**, 197–225.

68 D. P. August, S. Borsley, S. L. Cockroft, F. della Sala, D. A. Leigh and S. J. Webb, *J. Am. Chem. Soc.*, 2020, **142**, 18859–18865.

69 Y. Li, L. Jia, X. Tang, J. Dong, Y. Cui and Y. Liu, *Mater. Chem. Front.*, 2022, **6**, 1010–1020.

70 Y. Sekiya, K. Shimizu, Y. Kitahashi, A. Ohyama, I. Kawamura and R. Kawano, *ACS Appl. Bio Mater.*, 2019, **2**, 1542–1548.

71 F. M. Hughes, Jr., C. D. Bortner, G. D. Purdy and J. A. Cidlowski, *J. Biol. Chem.*, 1997, **272**, 30567–30576.

72 S. P. Yu, *Prog. Neurobiol.*, 2003, **70**, 363–386.

73 S.-H. Park, I. Hwang, D. A. McNaughton, A. J. Kinross, E. N. W. Howe, Q. He, S. Xiong, M. D. Kilde, V. M. Lynch, P. A. Gale, J. L. Sessler and I. Shin, *Chem*, 2021, **7**, 3325–3339.

74 J. A. Malla, R. M. Umesh, S. Yousf, S. Mane, S. Sharma, M. Lahiri and P. Talukdar, *Angew. Chem., Int. Ed.*, 2020, **59**, 7944–7952.

75 S. Salvioli, A. Ardizzoni, C. Franceschi and A. Cossarizza, *FEBS Lett.*, 1997, **411**, 77–82.

76 S. T. Smiley, M. Reers, C. Mottola-Hartshorn, M. Lin, A. Chen, T. W. Smith, G. D. Steele and L. B. Chen, *Proc. Natl. Acad. Sci. U. S. A.*, 1991, **88**, 3671–3675.

77 S. S. Sabharwal and P. T. Schumacker, *Nat. Rev. Cancer*, 2014, **14**, 709–721.

78 L. A. Sena and N. S. Chandel, *Mol. Cell*, 2012, **48**, 158–167.

79 A. Rasola and P. Bernardi, *Apoptosis*, 2007, **12**, 815–833.

80 D. Lee, J. Ha, M. Kang, Z. Yang, W. Jiang and B. Y. S. Kim, *Adv. Ther.*, 2022, **5**, 2100189.

81 A. Mondal, S. N. Save, S. Sarkar, D. Mondal, J. Mondal, S. Sharma and P. Talukdar, *J. Am. Chem. Soc.*, 2023, **145**, 9737–9745.

82 P. S. Low, W. A. Henne and D. D. Doorneweerd, *Acc. Chem. Res.*, 2008, **41**, 120–129.

83 M. Fani, M.-L. Tamma, G. P. Nicolas, E. Lasri, C. Medina, I. Raynal, M. Port, W. A. Weber and H. R. Maecke, *Mol. Pharm.*, 2012, **9**, 1136–1145.

84 I. Biancacci, F. De Lorenzi, B. Theek, X. Bai, J.-N. May, L. Consolino, M. Baues, D. Moeckel, F. Gremse, S. von Stillfried, A. El Shafei, K. Benderski, A. Azadkhah Shalmani, A. Wang, J. Momoh, Q. Peña, E. M. Buhl, J. Buyel, W. Hennink, F. Kiessling, J. Metselaar, Y. Shi and T. Lammers, *Adv. Sci.*, 2022, **9**, 2103745.

85 C. Dutta, P. Krishnamurthy, D. Su, S. H. Yoo, G. W. Collie, M. Pasco, J. K. Marzinek, P. J. Bond, C. Verma, A. Grélard, A. Loquet, J. Li, M. Luo, M. Barboiu, G. Guichard, R. M. Kini and P. P. Kumar, *Chem*, 2023, **9**, 2237–2254.

86 M. S. Kaucher, W. A. Harrell and J. T. Davis, *J. Am. Chem. Soc.*, 2006, **128**, 38–39.

87 Y. Le Duc, M. Michau, A. Gilles, V. Gence, Y.-M. Legrand, A. van der Lee, S. Tingry and M. Barboiu, *Angew. Chem., Int. Ed.*, 2011, **50**, 11366–11372.

88 X. Shen, Q. Lu, T. Peng, Y. Zhang, W. Tan, Y. Yang, J. Tan and Q. Yuan, *J. Am. Chem. Soc.*, 2024, **146**, 19896–19908.

89 Q. Zhang, Q. Liang, G. Wang, X. Xie, Y. Cao, N. Sheng, Z. Zeng and C. Ren, *JACS Au*, 2024, **4**, 3869–3883.